

Hourglass sector zoning in metamorphic tourmaline and resultant major and trace-element fractionation

VINCENT J. VAN HINSBERG,^{1,*} JOHN C. SCHUMACHER,¹ STUART KEARNS,¹ PAUL R.D. MASON,² AND GERHARD FRANZ³

¹Department of Earth Sciences, University of Bristol, Wills Memorial Building, Queens Road, BS8 1RJ, Bristol, U.K.

²Faculteit Aardwetenschappen, Universiteit Utrecht, Budapestlaan 4, 3584 CD, Utrecht, The Netherlands

³Fachgebiet Petrologie, Technische Universität Berlin, D 10623 Berlin, Germany

ABSTRACT

A new type of sector zoning, with an hourglass shape, has been identified in metamorphic tourmalines that formed under a wide variety of physical and chemical conditions. The two sectors in the *c*-direction are not equivalent due to asymmetry in the crystal structure of tourmaline along the *c*-axis. The *c*⁺ sector is characterized by low concentrations of Ti, Ca, Mg, and Na, although Al is high, and has a pale (commonly blue or pale-green) color. Conversely, the *c*⁻ sector is low in Mg and Al, and high in Ca, Fe, and Ti (the latter two causing the dark-brown color of this sector). The *a*-sector has intermediate characteristics and probably approximates a sector-free tourmaline. Thin sectioning of these sector-zoned tourmalines perpendicular to the *c*-axis can produce three types of apparent radial zoning patterns: blue-green cores, dark-brown cores, or no distinct cores. These apparent cores will further vary in relative diameter depending on the sectioning level. Furthermore, “core” boundaries can be straight or ragged depending on whether the relative growth speeds for the different faces was constant or variable. These textures have been used to argue for a prograde or detrital origin of tourmaline cores. However, sector zoning is a more appealing explanation for most of these textures, and can further explain the textural resemblance among metamorphic tourmalines from highly variable bulk-rock composition, metamorphic history, and mineral paragenesis. The sector zoning that is described here develops by preferential uptake of elements on the *r* growth plane, resulting from a combined effect of differences in surface charge and morphology of this plane in the *c*⁺ and *c*⁻ directions. This leads to the preferential incorporation of more positively charged elements in the *c*⁻ direction, and a preference for a vacant X-site in the *c*⁺ direction. Because the compositional differences among the sectors are pronounced in both major and trace elements and in the same order of magnitude as growth zoning variability, the presence of sector zoning must be established and taken into account when making inferences from tourmaline chemistry.

Keywords: Hourglass, sector zoning, tourmaline, metamorphic rocks, element fractionation

INTRODUCTION

Tourmaline, with the general formula $XY_3Z_6T_6O_{18}(BO_3)_3V_3W$ (Hawthorne and Henry 1999) is the most common B-mineral in metamorphic rocks (Henry and Dutrow 1996), and generally, especially at high grade, its dominant B reservoir. It commonly shows (complex) optical and chemical zoning, which is generally described in terms of core-rim zoning as the customary section used to study this zoning is perpendicular to the long (*c*) axis. Tourmalines from metamorphic pelites, gneisses, and metabasites seem to be ubiquitously characterized by an abrupt color change from core to rim (Tracy 1982; Henry and Guidotti 1985; Keller et al. 1999; Henry and Dutrow 2001; Kawakami 2001; Nakano and Nakamura 2001; Deksisssa and Koeberl 2002; Medaris et al. 2003; Bebout and Nakamura 2003). Generally, this is either a change from a blue-green core to a green-brown rim or from a dark-brown core to a green-brown rim. These color

variations are remarkably constant over a variety of metamorphic conditions, mineral parageneses, and bulk-rock compositions. Electron microprobe analyses have consistently shown that this abrupt change in color is accompanied by strong compositional changes (Tracy 1982; Henry and Guidotti 1985; Keller et al. 1999; Henry and Dutrow 2001; Kawakami 2001; Nakano and Nakamura 2001; Deksisssa and Koeberl 2002; Medaris et al. 2003). The compositional variations are generally step-like from core to rim and can be recognized in most major, minor, and trace elements.

In pegmatitic tourmaline, sector zoning is a common phenomenon (e.g., Rustemeyer 2003); however, sector zoning in metamorphic tourmalines is less well documented. Henry et al. (1999) described sector zoning in tourmalines from the cap rock of a salt dome and several authors have reported faceted sector zoning in cross-sections cut perpendicular to the *c*-axis (Tindle et al. 2002; Torres-Ruiz et al. 2003; Deksisssa and Koeberl 2002). Sector zoning is, in fact, a common phenomenon in many metamorphic minerals, such as chloritoid, staurolite, omphacite,

* E-mail: V.J.vanHinsberg@gmx.net

andalusite (variety chiastolite), zoisite, sphene, zircon (Watson and Liang 1995; Watson 1996 and references therein), and even quartz (Onasch and Vennemann 1995).

Tourmaline composition changes as a function of pressure, temperature, and its chemical environment, where the latter is in turn controlled by mineral paragenesis, local bulk composition, and fluid composition (which can be controlled externally). Changes in P , T , or bulk composition (i.e., metasomatism) lead to gradual changes in composition as the mineral assemblage readjusts its composition to the new conditions. Changes in the mineral assemblage, on the other hand, will result in more sudden changes in composition. The abrupt changes in color and composition between core and rim have therefore mainly been attributed to a sudden change in the host rock's mineral paragenesis (Tracy 1982).

Opponents of this explanation of core-rim color zones in metamorphic tourmaline note that the composition of these cores commonly is more-or-less homogeneous without signs of compositional growth zoning, although the rims are distinctly zoned. The presence of homogeneous cores and zoned rims is not consistent with continuous growth, and to account for

this observation, homogenization prior to rim growth has been proposed. Such a homogenization event is generally assumed to take place at the thermal peak of metamorphism, resulting in a prograde core and retrograde rim assignment for these tourmalines (Bebout and Nakamura 2003). However, these assignments are commonly difficult to reconcile with textural relationships, which suggests tourmaline formation to be early and prograde. Further objections to a prograde core interpretation are based on the textures of the core-rim boundary. Although this boundary can be euhedral in shape, it is commonly highly irregular, resulting in asymmetric cores. Additionally, within a single sample, the relative diameter of core vs. the width of the rim is highly variable within a tourmaline population of identical cross-sectional

TABLE 1. Sample origin and metamorphic conditions for the tourmalines used in this study

Sample	Origin	Rock type	Peak P and T
MC	Desges tectonic window, Massif Central, France	staur-garn-sill metapelitic schist	7 kbar, 650 °C
SY	Kini Peninsula, Syros, Cyclades, Greece	glauc-omph meta-gabbro	15 kbar, 500 °C
KW	Lower Schieferhülle, Tauern window, Austria	mafic chlorite-schist	6–8 kbar, 520–600 °C

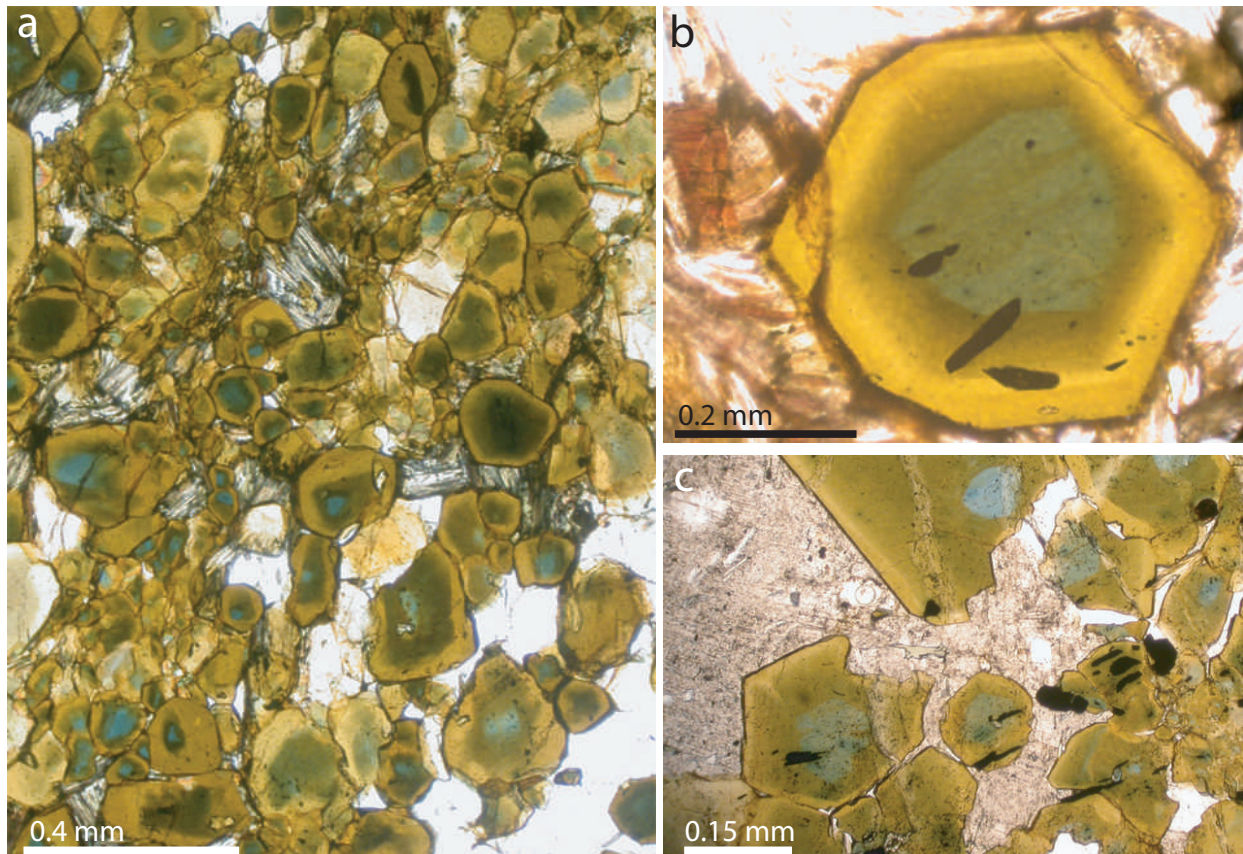


FIGURE 1. Plane-polarized photomicrographs of a tourmaline-rich band in sample MC28.5 (French Massif Central), showing cross-sections perpendicular to the c -axis. (a) The tourmalines have blue or dark-brown cores surrounded by a light-brown rim of various relative size. In some sections, a core appears to be absent altogether. Boundaries between core and rim are generally irregular. These textures can be taken to indicate a varied detrital origin for the tourmaline cores, with metamorphic overgrowths. However, **b** and **c** show ilmenite inclusions in the same sample overgrown by tourmaline, with individual ilmenites protruding from core to rim. Such a texture seems inconsistent with a detrital core origin, as this is unlikely to survive sedimentary transport.

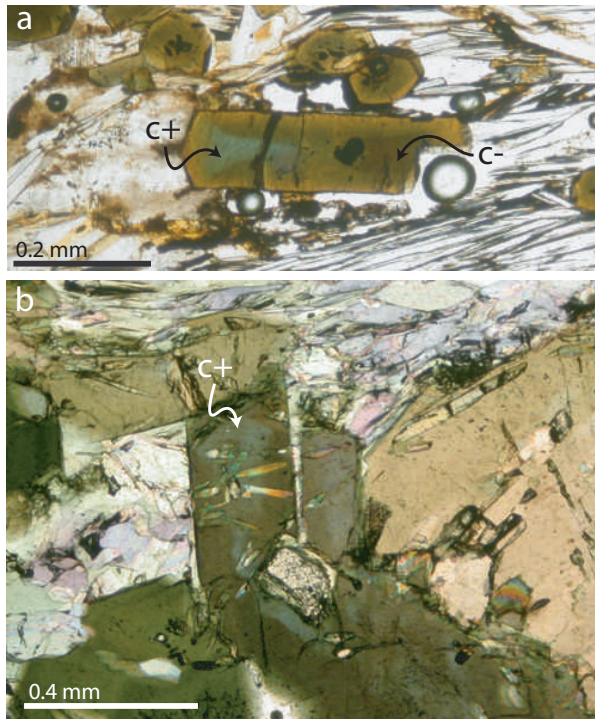


FIGURE 2. Plane-polarized photomicrographs of tourmaline grains from the French Massif Central (a, sample MC28.3) and Syros, Greece (b, sample SY4) sectioned parallel to their c-axis. Three color zones can be recognized in the Massif Central sample: a blue wedge on the c⁺ side of the crystal, a dark-brown wedge on the c⁻ side, and a light-brown zone in between. The Syros sample only displays the blue c⁺ zone because it has nucleated on another tourmaline grain. The boundaries between the different zones are diffuse and irregular, and cut by epidote inclusions in sample SY4.

diameter, and it is not uncommon to find a variety of core colors in the same sample. These observations, among others, have led to a proposed detrital origin for these cores, where only the rims represent growth during metamorphism (Henry and Guidotti 1985 and references therein).

Although the detrital core theory can explain many of the observations, detrital cores fail to satisfactorily explain the widespread occurrence and textural similarity, given the wide range in bulk compositions, metamorphic conditions, and geotectonic setting in which this particular core-rim zoning has been observed. In this paper, we present the results of a detailed study into compositional zoning in metamorphic tourmalines and the underlying mechanisms responsible for zoning. We will show that a correct interpretation of tourmaline zoning is only possible if a three-dimensional picture of the zoning is obtained.

METHOD

Tourmalines from three distinct areas were studied, covering a range of metamorphic conditions, bulk-rock compositions, and geotectonic setting (Table 1). Tourmaline grains of a range of sizes for each sample were separated by crushing to <2 mm and hand-picking, and were subsequently mounted in epoxy resin in sections both parallel and perpendicular to the long axis of the grains. Thin-sections were also prepared for all samples. Tourmalines in both grain mounts and thin-sections were WDS element-mapped on a Cameca SX-100 microprobe. At the Department of Earth Sciences, University of Bristol (UoB), element mapping was conducted at 20 kV, 150 nA for Mg, Fe, Ca, Ti, Al, Si, and Na, using a focused

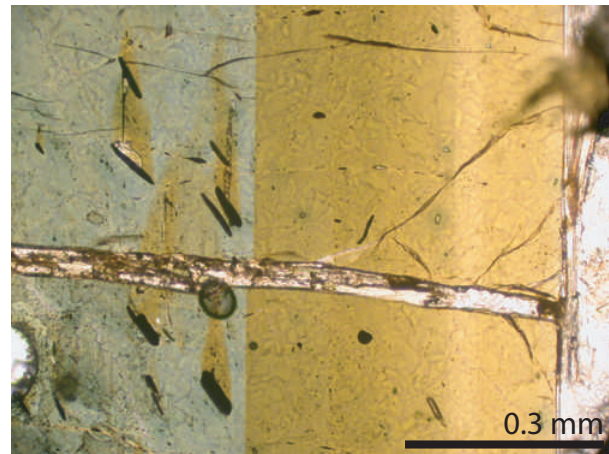


FIGURE 3. Plane-polarized photomicrograph of a tourmaline crystal (sample MCEOP008) sectioned parallel to its c-axis; c⁺-side is toward the top of the photograph. Growth zoning can be recognized by the color variations from core to rim and a sharp transition is present between the blue core zone and the brown rim. The core contains several opaque ilmenite inclusions, all with a shadow of brown tourmaline in the growth direction. This texture suggests that the inclusions “shielded” the region behind them causing tourmaline of rim color to grow. The crack running perpendicular to the long axis of the tourmaline grain results from late-stage extensional brittle deformation and is filled with quartz, chlorite, and a second generation of tourmaline.

beam. Background correction was applied by subtracting an average background count rate determined from multiple analyses on the center of the tourmaline grains, while assuming it to be constant over the complete grain. Spot and transect analyses were conducted by WDS on a Jeol-8600 probe at UoB at 20 kV, 20 nA with focused beam, using the following standards; wollastonite (Ca), olivine (Si), diopside (Mg), hematite (Fe), albite (Na), SrTiO₃ (Ti), orthoclase (K + Al), MgF₂ (F), and MnO (Mn). A ZAF correction, taking a fixed concentration of B₂O₃ (10.5 wt%) and H₂O (2.5 wt%) into account, was applied to all analyses. The 1 σ counting statistical relative error on the tourmaline analyses is SiO₂ 0.7, Al₂O₃ 0.7, TiO₂ 1.5, FeO 1.4, MgO 1.2, CaO 1.7, Na₂O 3.6, and F 1.5%, and for the trace elements K and Mn, 37 and 44% respectively. Detection limits (in weight percent) are SiO₂ 0.07, Al₂O₃ 0.07, TiO₂ 0.02, FeO 0.04, MgO 0.05, CaO 0.02, Na₂O 0.05, F 0.01, K₂O 0.02, and MnO 0.03%. Trace-element analyses were performed on a Geolas 193 nm excimer laser ablation system coupled to a Micromass Platform quadrupole ICP-MS, at the Faculty of Earth Sciences, Utrecht University using a 60 μ m diameter crater and fluence of 10 J/cm². Data were calibrated against NIST SRM 612 glass, with Ca (determined by EMP) as an internal standard. Accuracy was assessed by analyzing (with a crater size of 100 μ m) the dravite, schorl, and elbaite standards of Dyar et al. (2001) and was better than 10% for minor elements and better than 25% for trace elements, although repeated analyses for Zn on the schorl and Ni on the elbaite standard showed systematically lower values than those reported by Dyar et al. (2001). Precision was determined from repeated analyses of NIST SRM 612 glass bracketing the tourmaline analyses and was less than 5% RSD for all elements. Detection limits for the trace-element analyses are variable due to fluctuations in the background. The median detection limits for the analyses reported here are V 0.5, Ni 2.5, Zn 4.2, Sr 0.3, Pb 0.3, La 0.10, Ce 0.08, and Eu 0.14 ppm.

Tourmaline EMP analyses have been normalized to 15 cations excluding the alkalis, i.e., assuming no vacancies or B to be present on the Y, Z, or T sites. Elements have been distributed over the sites as follows; Si occupies the T site with any deficit made up by Al. The Z site is fully occupied by Al with any remaining Al residing on the Y site. Mg, Mn, Fe, and Ti occupy the Y site and the alkalis (Ca, Na and K) reside on the X-site. Vacancies are calculated from 1 minus the sum of the alkalis.

RESULTS

The tourmalines studied here are euhedral black to dark-brown crystals, occurring as isolated grains aligned subparallel

TABLE 2. Laser ablation ICP-MS trace element transect from the blue core of a tourmaline grain (sample MCVH30) to its brown rim (values in ppm)

analysis	Rel. pos.	V	Error	Ni	Error	Zn	Error	Sr	Error	La	Error	Ce	Error	Eu	Error	Pb	Error
T1-1	2	n.d.		n.d.		n.d.		n.d.		<0.09		<0.08		0.2	0.1	30	3
T1-2	1	n.d.		n.d.		584	70	n.d.		<0.10		0.6	0.1	<0.10		25	2
T1-3	12	n.d.		n.d.		221	27	n.d.		0.8	0.2	2.6	0.3	0.9	0.2	25	2
T1-4	3	79	7	37	15	559	87	66	5	<0.08		<0.09		<0.20		32	4
T1-5	4	86	7	56	20	618	91	72	6	<0.10		<0.07		0.2	0.1	25	3
T1-6	5	96	8	61	24	590	92	67	5	<0.11		<0.10		<0.14		25	3
T1-7	6	77	6	65	23	634	91	60	4	<0.11		<0.10		<0.20		21	2
T1-8	7	111	5	43	12	464	52	101	5	<0.07		0.2	0.1	0.2	0.1	47	3
T1-9	8	143	10	25	11	524	84	109	7	0.2	0.1	0.2	0.1	<0.14		47	5
T1-10	9	159	11	21	9	511	74	108	7	0.9	0.2	0.2	0.1	<0.20		51	5
T1-11	10	152	9	25	9	518	72	114	6	0.3	0.1	0.8	0.2	0.2	0.1	51	5
T1-12	11	156	10	36	13	445	64	108	7	0.5	0.1	1.3	0.2	0.4	0.2	46	4
T1-13	12	116	7	24	9	105	17	60	4	1.2	0.2	1.2	0.2	0.7	0.2	29	3
T1-14	12	145	10	30	11	107	19	66	5	0.2	0.1	1.6	0.3	0.8	0.3	37	4

Notes: Analyses have been calibrated against NIST SRM glass 612, with Ca (determined by EMP) as an internal standard. "rel. pos." refers to the relative position of the analysis spots with position 12 at the rim of this tourmaline grain. The transition from the blue core to the brown rim is between analyses T1-7 and T1-8. Errors are reported as absolute 1 sigma count statistical error. Where values were below the detection limit, the respective limit is given. "n.d." refers to values that were not determined in that specific run.

to the foliation. In the schist samples, they are concentrated in the micaceous bands, and local enrichments around quartz segregations can be found in the Massif Central samples. The grains range in size from <1 mm across to 2 mm in diameter and more than 2 cm long. In some samples, late-stage deformation has resulted in brittle extensional fractures perpendicular to the long axis (c) with a second generation of tourmaline growing on the fracture surface.

All crystals are distinctly zoned, both in sections cut perpendicular and parallel to the c-axis of the tourmaline grains. In perpendicular-to-c sections, the Massif Central (MC) samples have highly irregular cores, either blue or dark-brown in color, with light-brown euhedral rims (Fig. 1). The cores in the Tauern Window (KW) samples are blue with olive-colored rims and the Syros (SY) samples have blue-green or dark-green cores with olive-colored rims. Sections parallel to the c-axis show a different texture, with wedge-shaped zones on either side of the crystal, occasionally forming an hourglass shape. In complete tourmaline crystals, this hourglass consists of a blue wedge on one side of the grain, a dark-brown or green wedge on the other side, and a light-brown or olive-colored zone on either side (Fig. 2).

Abundant inclusions are present in the tourmalines, dominated by ilmenite, quartz, zircon, and monazite in MC samples, and epidote, chlorite, and less commonly omphacite in SY samples (Figs. 1 and 2). Commonly, these inclusions are aligned and preserve the preferred orientation of an older foliation overgrown by tourmaline (Fig. 1c). In places, inclusions can be found that protrude from the light- or dark-colored core of tourmaline grains into their rim (e.g., Figs. 1b and 2b). Another interesting feature related to inclusions is the presence of "shadows" next to inclusions in sections parallel to the c-axis (Fig. 3). These shadows have so far only been observed in the blue zones, and invariably have a wedge-shaped brown tourmaline "overgrowth" in the growth direction.

Element maps (Fig. 4) show a similar texture to the optical zoning, with concentric zoning observed in sections perpendicular to the c-axis and hourglass zones in sections parallel to c. The element zoning is especially clear for Ca and Ti, where overall relative differences in composition are most pronounced (Fig. 4), and is much less evident in Fe and Si. In some element

maps, a distinct heterogeneity is present within the hourglass zones (e.g., Figs. 4a and 4b). Quantitative EMP analyses show that these tourmalines are schorlitic to dravitic in composition [$\text{NaFe}_3\text{Al}_6\text{Si}_6\text{O}_{18}(\text{BO}_3)_3\text{OH}_4$ to $\text{NaMg}_3\text{Al}_6\text{Si}_6\text{O}_{18}(\text{BO}_3)_3\text{OH}_4$], with limited substitution toward the foitite [$\square\text{AlFe}_2\text{Al}_6\text{Si}_6\text{O}_{18}(\text{BO}_3)_3\text{OH}_4$, <20%], olenite [$\text{NaAl}_3\text{Al}_6\text{Si}_6\text{O}_{18}(\text{BO}_3)_3\text{OH}_4$, <20%], and uvite [$\text{CaMg}_3\text{MgAl}_6\text{Si}_6\text{O}_{18}(\text{BO}_3)_3\text{OH}_4$, <10%] end-members (a table with all EMP analyses reported in this study is available as supplementary material¹).

Trace-element analyses indicate a strong influence of zoning on trace-element content with distinct variations between different zones (Table 2). The REEs (La, Ce, and Eu) show a strong, approximately tenfold increase from core to rim. Zinc, at concentrations ranging from 450 to 900 ppm is the most abundant trace element in the MC samples studied, but shows little variation.

DISCUSSION

Sector zoning in tourmaline

The hourglass zoning observed in complete tourmaline crystals from these three localities is similar to hourglass zoning observed in magmatic clinopyroxenes and metamorphic staurolites (Hollister and Gancarz 1971; Hollister 1970). Although sector zoning has been reported previously in tourmalines, as mentioned in the introduction, this is (to the best of our knowledge) the first reported find of hourglass sector zoning in tourmaline.

Unlike the hourglass sector zoning observed in staurolite and clinopyroxene, the two sectors in the c-direction in tourmaline are not equivalent in color and composition (Figs. 2 and 4). This difference results in three distinct sectors for every tourmaline

¹ Deposit item AM-06-016, Supplementary Table. Deposit items are available two ways: For a paper copy contact the Business Office of the Mineralogical Society of America (see inside front cover of recent issue) for price information. For an electronic copy visit the MSA web site at <http://www.minsocam.org>, go to the American Mineralogist Contents, find the table of contents for the specific volume/issue wanted, and then click on the deposit link there.

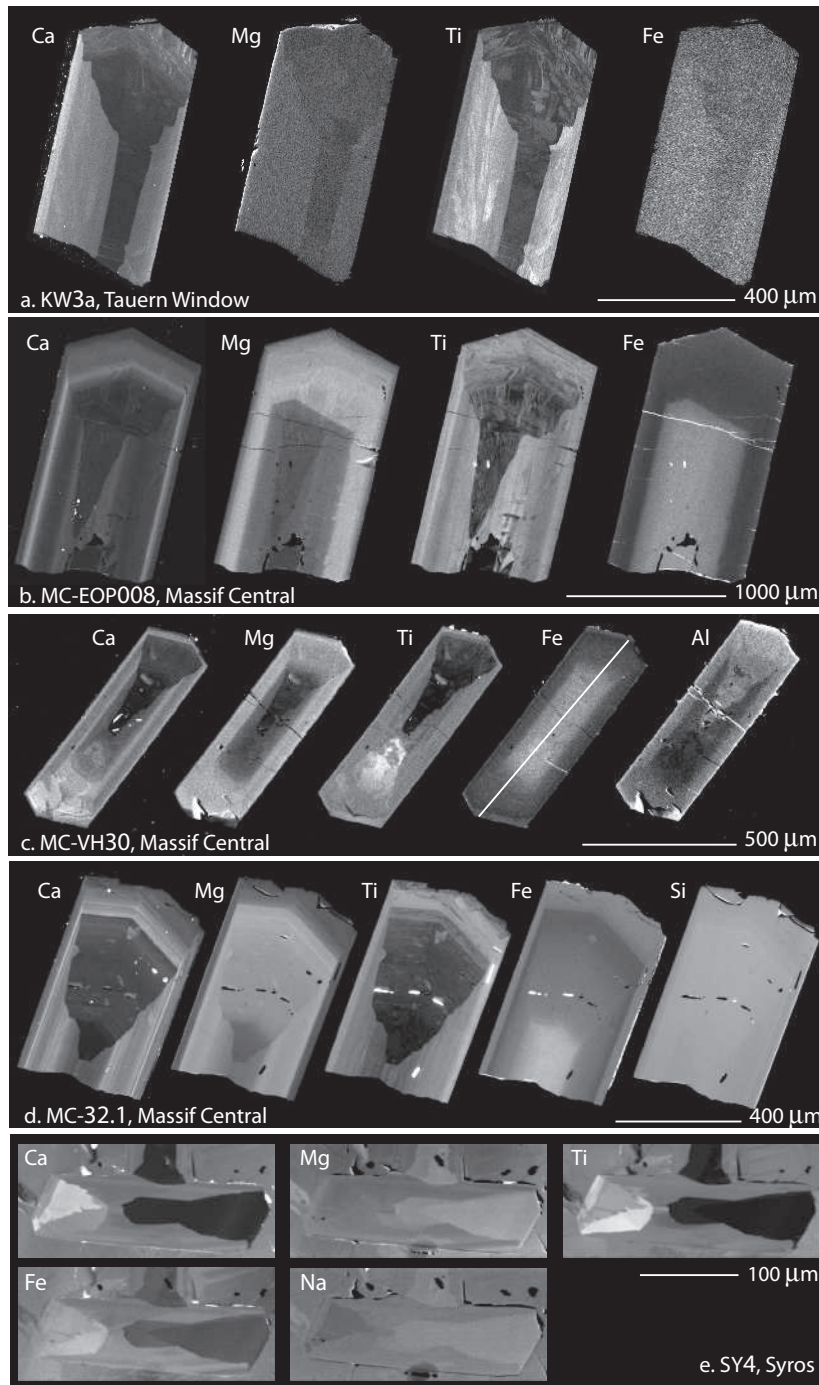


FIGURE 4. Electron microprobe wavelength dispersive element X-ray maps for tourmaline crystals from the Tauern Window (a), the French Massif Central (b, c, d), and the Cyclades island of Syros (sample SY4) sectioned parallel to the *c*-axis. Distinct compositional zoning can be recognized in these sections, outlining hourglass sectors. The differences between the sectors converge from core to rim and approach the composition of the intermediate sector. The Syros sample (e) displays five sectors instead of three, which is interpreted to result from the interaction of two sector-zoning directions. Boundaries between the sectors are commonly irregular and compositional heterogeneity within sectors can also be observed.

growth zone. This asymmetry along the *c*-axis results from the absence of any crystal-symmetry elements perpendicular to the *c*-axis of the crystal, which also displays itself in the piezoelectric and pyroelectric behavior of tourmaline (Donnay 1977 and references herein) and in different crystal habits on the two *c*-axis terminations (Henry and Dutrow 1996). A *c*⁺ and *c*⁻ assignment is used to distinguish the two directions (Barton 1969), where the antilogous pole is the *c*⁺ and the analogous pole is the *c*⁻ side of the crystal (assignments used are shown in Fig. 5).

This asymmetry in the *c*-direction has further been inferred to

account for the compositional disparity observed in overgrowths on the *c*⁺ and *c*⁻ sides of existing tourmalines (Sperlich 1990; Sperlich et al. 1996; Henry and Dutrow 1992, 1996). These overgrowths are in fact similar to the hourglass sector zoning observed in this study, in that the compositions and color of the tourmaline overgrowth in two *c*-directions are markedly different. The *c*⁺ overgrowths are characterized by a pale-blue to green color, with relatively low concentrations of Ti and Ca, whereas the *c*⁻ overgrowths are brown and relatively rich in Ca and Ti (Sperlich 1990; Sperlich et al. 1996; Henry and Dutrow 1992,

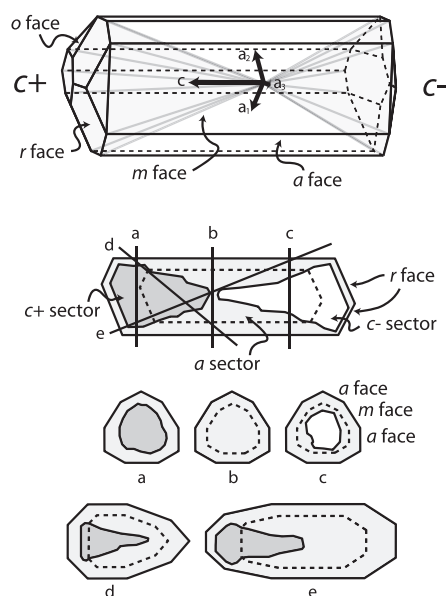


FIGURE 5. Schematic drawing and cross-sections through an hourglass sector-zoned tourmaline crystal, outlining the sector and crystal-face definitions used throughout this paper. **r** and **o** crystal faces are found as the terminating pyramidal faces on the tourmalines studied here, although the **m** and **a** faces make up the prism faces parallel to the **c**-axis. The **c**⁺ sector is characterized by pale colors, commonly blue-green, but the **c**⁻ sector is much darker in color. The intermediate sector will be referred to as the **a**-sector throughout this paper, as no differences were apparent among the **a**₁, **a**₂, and **a**₃ growth directions. The various cross-sections through this hourglass sector-zoned crystal show that markedly different sections can result from a single sector-zoned crystal. (Figure modified after Sperllich et al. 1996.)

1996), which is identical to what we observe for sector zoning in the **c**⁺ and **c**⁻ directions.

The Syros samples have a further division in the **c**⁺ and **c**⁻ sectors, bringing the total number of sectors to five (Fig. 4e). We believe this splitting of the **c**-sectors to result from superposition of two sector-zoning directions, both operating sub-parallel to the **c**-axis, and possibly similar to the two directions (**r** and **o**) found by Henry et al. (1999). The apparent overlap between the split sectors on either side of the tourmaline grain and the asymmetry between their **c**⁺ and **c**⁻ expression probably results from the sectioning orientation. A backscattered-electron image of a tourmaline grain from the same sample that was sectioned perpendicular to the **c**-axis, does indeed show regular splitting of the sector, without overlap (Fig. 6).

Compositional effects of sector zoning

Sector zoning develops when elements are preferentially incorporated on specific growth surfaces and these differences survive in the bulk crystal. Local equilibrium between the mineral surface and its environment is attained, even though these equilibria will be different for the various growth faces or sectors. Once the growth face progresses, and the different sectors find themselves in the bulk crystal, they are no longer in equilibrium,

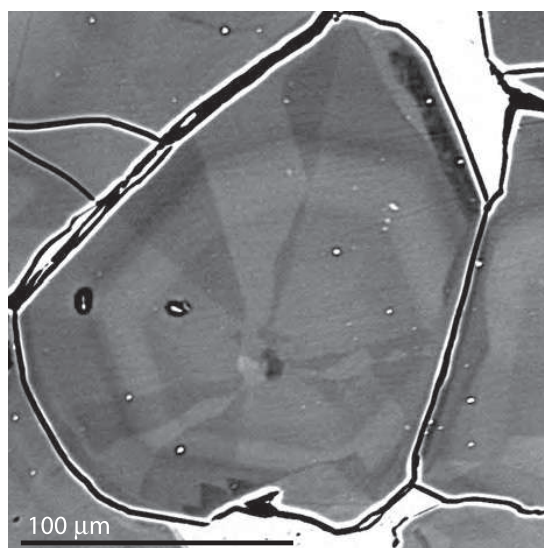


FIGURE 6. Backscattered-electron image of a tourmaline crystal (sample SY4), sectioned perpendicular to **c**. The image shows faceted compositional sector zoning splitting the crystal into two different compositions, with concentric growth zoning superimposed on the sectors.

as inside the crystal the crystallography is identical for all directions. Differences will normally be eliminated by diffusion, and it is only the inferred slow diffusion rates in tourmaline (Voll 1969; von Goerne et al. 1999) that allow this zoning to survive in tourmaline.

The extent of the compositional differences among the three sectors can be gauged from the element maps (Fig. 4). Clear differences are present among the sectors within any given growth zone, and the strongest differences are present between the **c**⁺ and **c**⁻ sectors. To properly assess the effects of sector zoning, only differences within a given growth zone can be compared, as the overall compositional differences will be a combination of sector and growth zoning (e.g., the Ca rich band in Fig. 4c). A microprobe traverse taken roughly parallel to the **c**-axis of a tourmaline crystal from sample MCVH30 (Fig. 4c) shows the extent of these differences (Fig. 7). Traversing from the **c**⁺ sector into the **c**⁻ sector, there is a sharp step in element concentrations. The most pronounced differences are in Ca and Ti, but differences are also distinct in the other elements. In fact, a statistical analysis of the Si, F, and K count rates shows that these are also significantly different among sectors at the 1% confidence interval level. This is especially interesting in terms of Si, as it validates non-stoichiometric Si contents on the T-site.

Besides the strong relative compositional differences between the sectors, the profile also shows compositional variations within the sectors that are related to growth zoning. Both sectors are similar in this respect and show the same systematic variations from core to rim. These variations will be related to changes in the tourmaline growth environment in terms of *P*, *T*, and local element mobility. The two dominant exchange vectors (eigenvalue > 1) that emerge from a factor analysis of the data in this profile are a Mg ↔ Fe exchange and a Na + (Mg,Fe) ↔ □ + Al exchange (Fig. 8). Both these substitutions are, in fact, so

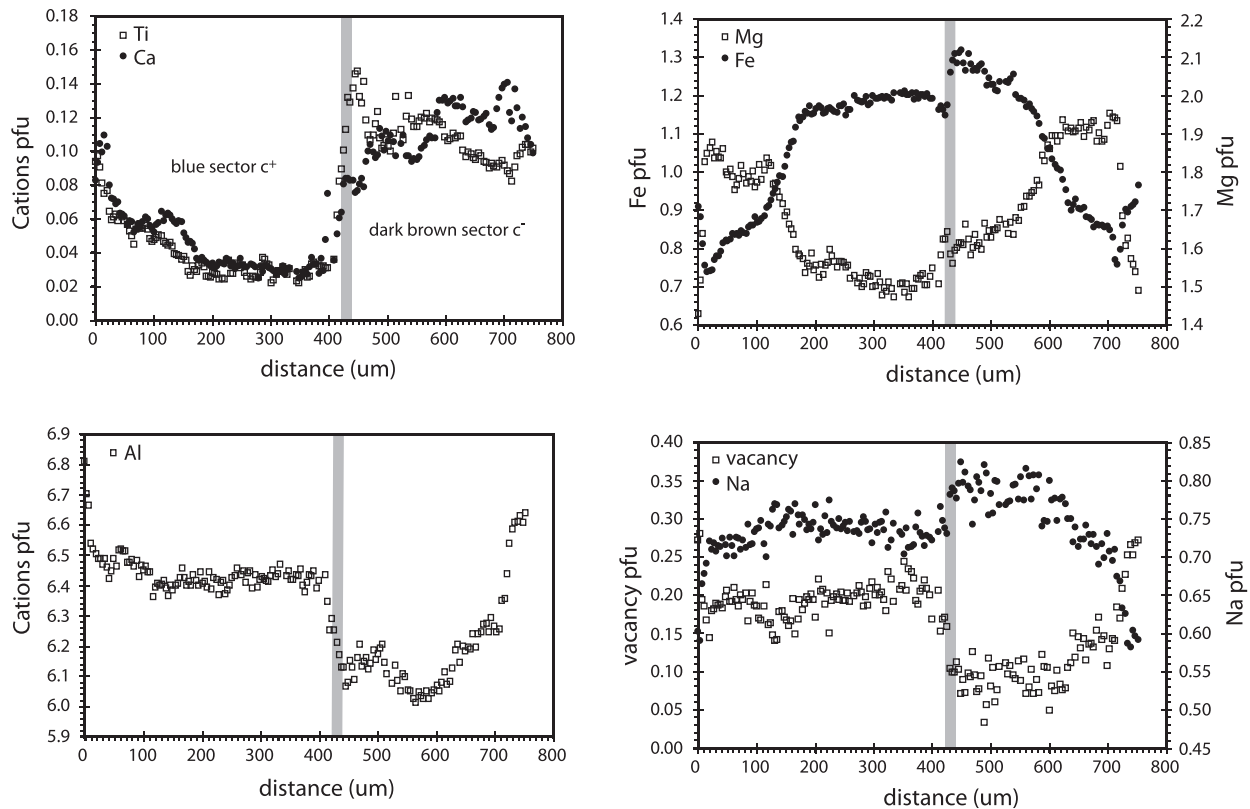


FIGURE 7. Chemical profiles along the long axis of a tourmaline grain (sample MCVH30, profile line shown in Fig. 4c), measured by electron microprobe. Inclusions have been removed from the data set. Traversing from the c^+ sector into the c^- sector, there is a clear compositional step that can be recognized in all elements, although it is most pronounced for Ca and Ti. Note that the c^- sector in this crystal is heterogeneous (Fig. 4c) due to the presence of several surface cracks.

pronounced that exchange vectors for the other elements cannot be resolved, as they are generally linked to components in the two main element exchanges.

As can be seen in Figure 7, as well as in the color differences among sectors in Figure 4, the compositional differences among sectors diminish from core to rim. In fact, in the Massif Central samples, the differences in the final growth zone are negligible, and show a trend that diverges from the behavior of either sector (Fig. 9). Sperlich et al. (1996) and Henry and Dutrow (1996) found a similar decline in the differences between corresponding overgrowths on the c^+ and c^- side of tourmaline grains, which they correlated with an increase in metamorphic grade, mainly temperature. Such an explanation is appealing for sector-zoning as well, as the preference for certain elements to attach to specific growth surfaces can be expected to diminish with increasing temperature. This is not unlike the increased tolerance of minerals to incorporate normally incompatible elements in their crystal lattice at elevated temperatures. Any systematics in the compositional differences among sectors with temperature would be a valuable tool for geothermometry as suggested by Henry and Dutrow (1996) for polar overgrowths.

The elements involved in tourmaline sector zoning are present at all sites of the generalized tourmaline formula of $XY_3Z_6T_6O_{18}(BO_3)_3V_3W$ (from Hawthorne and Henry 1999), and suggest that all sites are involved and affected by sector zoning.

To determine the element preference of the different sectors and the substitutions involved, the sectors have to be compared to their non-sector zoned equivalent. We believe that the a -sector (Fig. 5) represents the closest analog to such a composition (details below). Comparing the c -sectors with the a -sector in terms of element content shows a preference for Ca, Ti, and Fe in the c^- sector accompanied by a lower Mg concentration. The c^+ sector, on the other hand, has a preference for Al and X-site vacancies and distinctly lower concentrations of Ti, Ca, Na, and Mg. The element signature for the two sectors indicates that they are not a mirror image of each other, but rather prefer specific elements. In the c^- sector, Ti and Fe substitute for Mg, although the exchange vector is not well-defined and appears to also include Al. Calcium appears to substitute for \square on the X-site, as the Na content is like that of the a -sector. For the c^+ sector, differences are more pronounced, with Al substituting for Mg and Ti on the octahedral sites and vacancies replacing Ca and Na on the X-site. These substitutions will also be accompanied by changes of the O:OH ratios on the V and W sites to preserve charge balance, but the present analyses do not allow for assessment of this effect.

The decoupling of Fe and Mg in the c -sectors suggests that the Y and Z sites are affected differently by sector zoning. Hawthorne and Henry (1999) and Hawthorne (2002) distributed Al and Mg over both the Y and Z sites, although Fe appears to be restricted

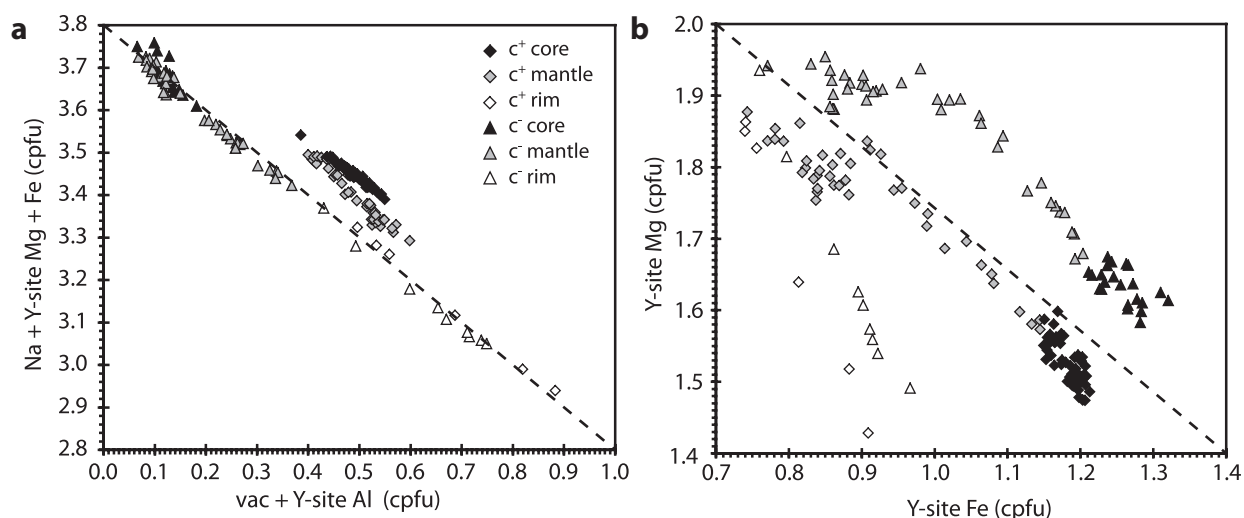


FIGURE 8. Composition of tourmaline (sample MCVH30, see also Fig. 7) in terms of cations per formula unit. The two dominant compositional exchanges operating are a $\text{Mg} \leftrightarrow \text{Fe}$ exchange and a $\text{Na} + (\text{Mg}, \text{Fe}) \leftrightarrow \square + \text{Al}$ exchange. The deviations from the 1:1 line in (a) result from variable presence of Ca on the X-site, which is enriched in the c⁻ sector compared to the c⁺ sector. (b) Shows similar behavior for both sectors, but with an offset in the Mg+Fe content. The rim composition for both sectors is indistinguishable and shows a distinctly different trend from the core and mantle of the two sectors, with decreasing instead of increasing values of X_{Mg} . This might suggest a prograde evolution for the sector-zoned region of this tourmaline, with a retrograde homogeneous rim.

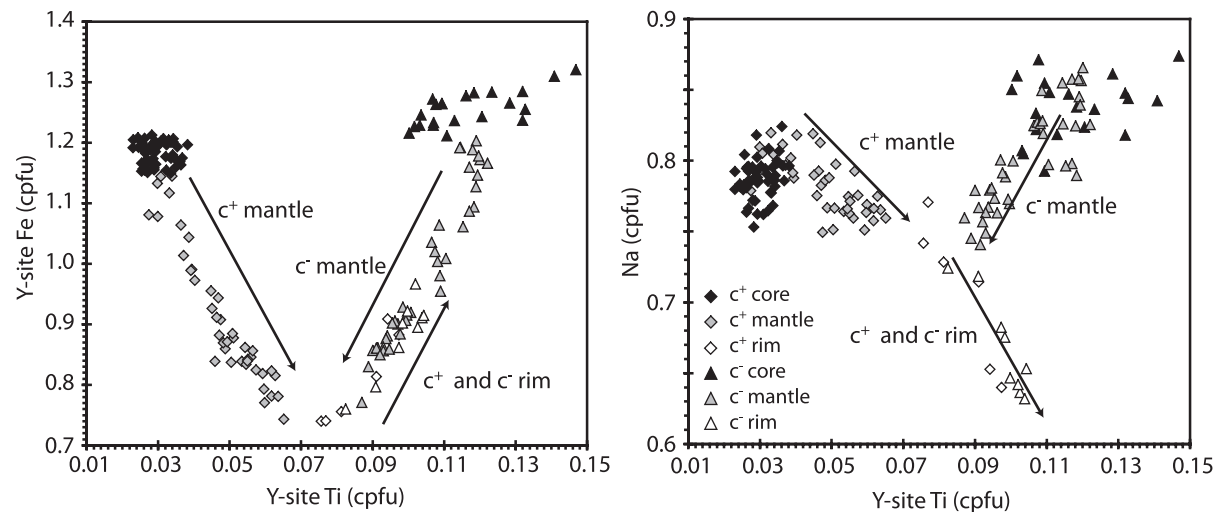


FIGURE 9. Composition of tourmaline (sample MCVH30, see also Fig. 7) in terms of cations per formula unit. Ti vs. Na and Fe show distinctly different trends for the two sectors in the c-direction, although both converge from core to rim. The actual rim itself shows no compositional differences between the two sectors and shows consistent, and markedly different behavior from the core and mantle regions.

to the Y-site. The lack of any compositional difference between c⁺ and a-sectors in terms of Fe suggests that sector zoning in this direction only includes the Z-site, although sector zoning in the c⁻ direction also affects the Y-site. Potentially this is also affected by a preference for trivalent Fe in one of the sectors.

The compositional differences among sectors are pronounced and are of the same order or larger than the compositional variations resulting from growth zoning (Figs. 7 and 9). For every growth zone, three distinctly different compositions are thus present, each representing and preserving local equilibrium between tourmaline and its environment at the time of growth. Any attempt to extract information about tourmaline growth

conditions must therefore take into account the effects of sector zoning.

Sector heterogeneity. The element maps for tourmalines from the Tauern window and for some of the tourmalines from the Massif Central show a distinct heterogeneity within growth zones. This heterogeneity is especially apparent for Ti, as can be seen in the Ti X-ray map for sample KW3a (Fig. 4a). Ti-rich and Ti-poor stringers can be observed, with varying orientations in different growth zones and corresponding concentration differences can be recognized in Ca, Mg, and Fe. The heterogeneity is most pronounced in the c⁺ sector. This compositional heterogeneity appears to reflect disequilibrium within these zones during

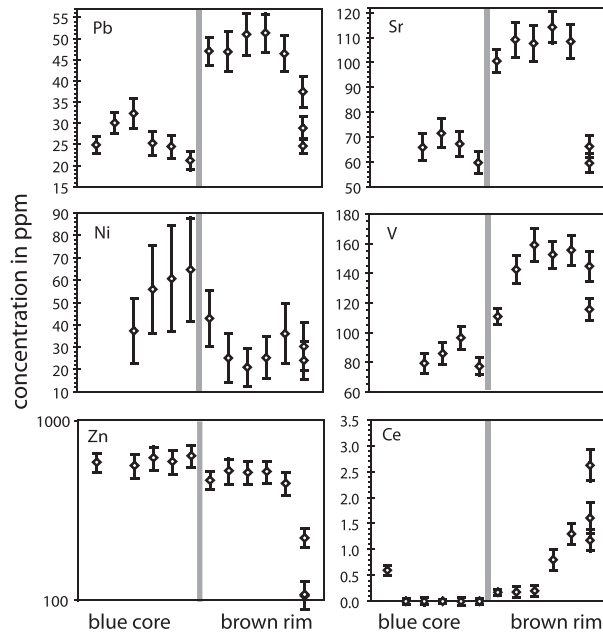


FIGURE 10. Trace-element profiles for a laser ablation ICP-MS transect (60 μm diameter craters at ~ 200 μm spacing) from the blue core of a tourmaline grain (sample MCVH30) to its light-brown rim. The core is more or less homogeneous as it represents a single-growth horizon, but the rim shows strong growth zoning, especially for Ce. Between core and rim there is a compositional step due to sector zoning in Sr, V, Ni, Zn, and Pb, and possibly in Ce, although this is concealed by its strong growth zoning. Count statistical errors are shown as 1 sigma. Note that Zn is plotted on a logarithmic scale.

growth, but we are unsure what is causing it. One possibility is that the compositional heterogeneity reflects original sample heterogeneity of the region later overgrown by tourmaline as has been invoked to explain Ti heterogeneity in garnet (Carlson 2002). In our case, the compositional heterogeneity could either reflect the compositions of the overgrown minerals (and possible heterogeneity therein) or heterogeneity in the bulk reaction volume due to different minerals being present along the growth surface (which may or may not take part in the reaction). Either explanation could result in different equilibria operating on different parts of the growth surface, preserved by low diffusion rates. This effect is most pronounced in the c direction, and could be related to the faster growth in this direction compared to the directions perpendicular to it.

Tourmaline color. The distinct differences in Ti content among the different sectors provide an explanation for the systematic color differences observed for zoned tourmalines from widely varying physicochemical conditions. In amphiboles, a temporary charge transfer between Fe^{2+} and Ti^{4+} results in Fe^{3+} and Ti^{3+} , which gives amphiboles a brown color (Litvin et al. 1986). We infer a similar mechanism for tourmaline and, consequently, the intensity of the brown color will depend on the concentrations of Fe and Ti. In the crystals studied here, Ti always will be limiting the charge transfer and the Ti concentration will control the intensity of the brown color. Indeed, this is what is observed for the different sectors. The c^- sector has the highest Ti

concentration and the darkest brown color and vice versa: the c^+ sector, with the lowest Ti sector, has the lightest color. Although the absolute concentrations of Fe-Ti are a function of bulk composition, P - T , and mineral assemblage, sector zoning will control the intracrystalline Ti and Fe distribution, and as such, control the color and color intensity for the different sectors.

Trace-element partitioning between sectors

Figure 10 shows the trace-element concentrations for a profile from the c^+ (pale-blue) core to the light-brown rim of a tourmaline crystal from sample MCVH30 sectioned perpendicular to the c -axis. The core of the crystal is fairly homogeneous within error, although the rim displays distinct differences related to compositional growth zoning. The absence of growth zoning in the blue core results from sectioning subparallel to the growth surface, as discussed below, and the core analyses thus represent a single compositional growth zone from this sector. The most pronounced growth zoning is present for the REEs, which show a tenfold increase from core to rim (see also Table 2). Given the slow diffusion rates observed for tourmaline (Voll 1969; von Goerne et al. 1999), this increase toward the rim cannot be related to post-growth diffusional enrichment, but must record a gradual increase in the mobility of REEs in the tourmaline growth environment.

Sector-zoning effects are pronounced for Sr, Pb, V, and Ni, and reveal themselves as steps in element concentration at the transition from core to rim (Fig. 10). Due to the strong growth zoning in the REEs, no definite sector-related difference between core and rim can be established. Comparing these trace elements with the behavior of the majors shows that Sr, Pb, and V follow Ca and Ti. Given their different (geo)chemical affinities, Sr and Pb probably follow Ca onto the X-site, whereas V follows Ti onto the Y-site. It is interesting that even the approximate twofold increase in the trace elements corresponds to the increase found in the major elements. Nickel, on the other hand, shows a decrease from core to rim and, as such, mimics the behavior of Mg in this specific sample. However, the sector effect is about two times more pronounced in Ni. Furthermore, semi-quantitative spot analyses in the c^+ sector and the rim adjacent to it, also reveal a distinct increase for Cu, Cr, and Sn, suggesting a decoupling between Cu and Ni. Interestingly, Zn, which is the most abundant transition metal in these tourmalines at 650 ppm, does not seem to be strongly influenced by sector zoning.

Sectioning effects of sector zoning

The presence of sector zoning in these samples provides an alternative explanation to the apparent inconsistencies in prograde vs. detrital core origins raised in the introduction of this work. The ubiquitous presence of both blue and dark-brown cores, and brown rims in tourmalines from widely different metamorphic terrains in terms of P - T , bulk composition, intergranular fluid composition, and mineral paragenesis, can all be reconciled by these representing different sectors in tourmaline. With sector zoning developing under all of these varying physicochemical conditions, similar core-rim textures will be present.

Furthermore, variable sectioning of sector-zoned crystals can explain the differences in relative core size and core color that are often observed in crystals of similar diameter, especially

in sections cut perpendicular to the c -axis (e.g., Fig. 1). When sectioning through the c^- sector, the crystals will appear to have a dark-brown core with a lighter colored rim, although sectioning through the c^+ sector will give a blue core instead. Sectioning precisely at the contact between the c^+ and c^- sectors will give crystals without a distinct core. Sectioning at different elevations through the crystal will further result in variable apparent core size, for any given diameter. Figure 5 schematically shows sections through different parts of a sector-zoned crystal, similar to the sectioning shown by Sperlich et al. (1996), who stressed its importance for compositionally asymmetrical overgrowths.

The growth systematics of hourglass sector zoning also can explain the irregular boundaries around cores that have been inferred to indicate a detrital origin. Because the interface between two sectors represents the intersection of two growth planes, its orientation will depend completely on the relative growth speeds, and hence growth mechanisms, of the two intersecting growth planes. If these relative speeds vary during growth, the intersecting plane will not be a straight line, but irregular. This can be seen clearly in Figures 2 and 4. Sectioning such an irregular surface will result in an irregular boundary between core and rim, which can easily be misinterpreted as a corroded detrital core.

The location of the section relative to the tourmaline c -axis also will determine the extent of growth zoning exposed in the different sectors. In a section that is cut perpendicular to the c -axis, compositional growth zoning in the rim will be fully displayed. However, the core sector will more or less display a single growth surface because growth occurs in a direction perpendicular to the thin-section plane. In contrast, a section parallel to the c -axis will show the compositional growth zoning in all sectors simultaneously and should therefore be preferred.

Inclusions provide a further textural observation that can compellingly be explained by sector zoning. In a sector-zoning case, core and rim represent growth at the same time, but in different directions. The ilmenite and epidote inclusions protruding from core to rim (Figs. 1b, 1c, and 2b) have thus been incorporated at the same time. Conversely, the presence or absence of specific inclusions in core or rim cannot be used directly to infer different formation conditions, because they may represent simultaneous growth.

Inclusions also can shield the growth region behind them leading to the formation of “shadows” with different composition and color (Fig. 3). There is no evidence for tourmaline nucleation on these inclusions, which suggests that growth in these regions takes place from the sides inward. This growth direction is identical to that of the rim and indeed composition and color of these “shadows” is indistinguishable from that of the rim.

The above is not intended to exclude detrital cores altogether. In fact, we strongly agree that detrital cores are an established phenomenon in tourmaline. However, several criteria that have been used to assign a detrital core origin to tourmaline cores can be explained equally well by hourglass sector zoning, and we therefore believe that alternative evidence has been sought to warrant assignment to either.

Crystallograph controls

Based on the exposed crystal faces of tourmaline and the faces preserved in compositional growth zoning and inclusion zones

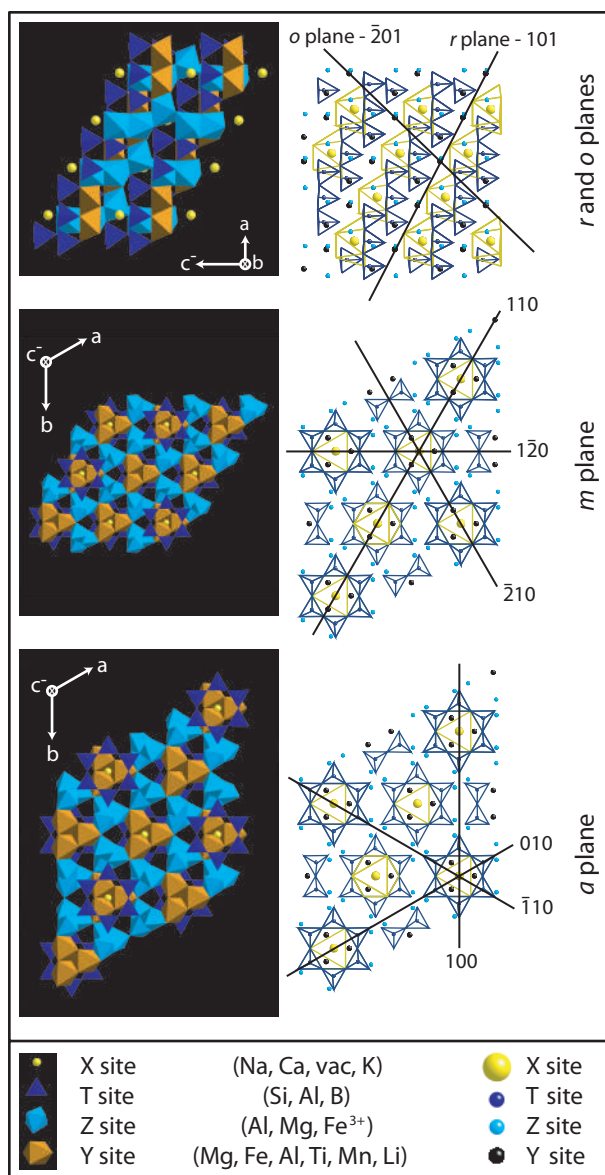


FIGURE 11. Crystallographic projections of the main growth faces operating in the tourmalines studied here. Growth in the c -direction takes place on the r -face and growth perpendicular to the c -axis on the m and a faces. The m and a faces have an internal mirror plane, but the r -face is distinctly different in the c^+ and c^- directions. The presence of a tetrahedron-ring with all tetrahedra pointing in the c^+ direction, results in a dipolar negative charge on the basal plane, giving the c^- direction a preference for more positively charged elements. The site morphology on the two r -faces is also distinctly different, especially for the X-site. In the c^+ growth direction, the X-site is exposed as an isolated site on a solid octahedral sheet, resulting in this site to be preferably vacant in this direction. The preferential uptake of an element on a growth face will place constraints on the morphological and charge preference of adjacent sites, and the observed element preference will thus represent an average of the element incorporations on a micro-scale. The absence of morphological or dipolar charge related element preference on the m and a faces suggests that these growth directions represent the tourmaline composition equivalent to a crystal not affected by sector zoning. These figures were prepared with CrystalMaker version 6.

in the samples studied here, we believe the dominant growing faces to be the **r**-plane {10-11} in the **c** direction, and the **m** {10-10} and **a** {11-20} planes perpendicular to the **c**-axis (Fig. 5). A large number of other possible growth faces in the **c**-direction is known for tourmaline (Ford and Dana 1932), however no remnants of these faces are preserved in the tourmalines studied here, except for rare **o**-faces on the terminations of well-formed tourmaline grains. Growth on any of the other planes would further be difficult to reconcile with the overall shape of the crystals, especially in light of the consistency in the **r**-face preserved in growth and inclusion zones inside the crystals. Growing faces are regarded here as the time- and space-average faces exposed during growth. However, intermediate growth faces of different orientation will be present, as building blocks are incorporated on the surface of the growing tourmaline. Because these faces are temporary, will vary with each growth step, and occur and coexist on a micro-scale, they are not considered here.

We believe sector zoning to result from differential uptake of elements on the various growing faces exposed, and we have therefore calculated the morphology and chemistry of the **r**, **m**, and **a** faces using the computer program CrystalMaker (version 6). A projection of each of the growing faces in a direction perpendicular to the plane is shown in Figure 11. The main difference between the **m** and **a** faces and their corresponding planes, and the **r** face is the lack of a mirror plane in the latter, resulting in the two opposite **r** growing faces to be different. The differences are especially clear in the morphology of the X-site, which occupies a cavity shielded by the sixfold Si-rings on the **c**⁻ side of the face, but sitting on a solid octahedral sheet on the **c**⁺ side (Fig. 11). This difference will result in different bonding energies for cations occupying this site on either side of the crystal with those on the **c**⁻ side being more strongly bound.

Furthermore, the structure of the Si₆O₁₈-ring with all tetrahedra pointing in the same direction parallel to **c**, results in an asymmetrical charge distribution, where the basal plane of the Si₆O₁₈-ring (**c**⁻ side) has a dipolar negative surface charge, whereas the plane containing the apical O atoms (**c**⁺ side) will have a positive dipole charge. This charge effect will lead to a stronger attraction of, or preference for positively charged elements on the **c**⁻ side of the **r** growth face. For the X-site, **c**⁻ preference would be Ca²⁺ or Na⁺ over a vacancy and for the octahedral sites this would be Ti⁴⁺. Similarly, the **c**⁺ **r**-surface will have a preference for more negatively charged elements, and hence prefer vacancies over Na⁺ and Ca²⁺ on the X-site. The Y and Z sites prefer Al over Mg and Fe (Fig. 7), which may seem counterintuitive. However, the presence of Al at either of these sites will be (partially) charge compensated by exchanging OH⁻ for O²⁻, thus giving the Al-octahedron a relative negative surface charge. Conversely, Mg and Fe will have a dipolar positive charge on one side of the octahedron, around the H atom. This interpretation does assume that the elements on the X-site are incorporated as individual cations, whereas the octahedral Y and Z site elements, including Al, Mg, Fe, and Ti, are absorbed onto the growth faces as octahedrally coordinated clusters.

Given that Ca and Ti have a full extra charge unit compared with the elements for which they exchange, preference would be expected to be most pronounced in these elements, and this is in fact what is observed (Figs. 4 and 7). Effects for Al, Mg, and

Fe are less pronounced, as their relative charge differences are only a fraction of a full charge unit. However, the disparity in Na behavior between **c** and **a**-sectors and the decoupling of Mg and Fe indicates that charge is not the only controlling factor, and site morphology must also play a role.

With increasing temperature the vibrational energies of the atoms will increase, resulting in a decrease of the dipolar charge on the Si₆O₁₈-ring. This decreasing charge will lead to a diminishing relative preference of elements for the **c**⁺ and **c**⁻ side of the **r**-face and explain the observed convergence of the sector compositions from core to rim, as well as the convergence in the asymmetrical overgrowth compositions reported by Sperlich et al. (1996) and Henry and Dutrow (1996).

Similar differences in site exposure and dipolar surface charge are absent for the **m** and **a** faces. In fact, the crystallographic differences between the **m** and **a** faces appear to be minimal, and compositional differences between **a** and **m** have indeed not been observed. The absence of a morphological or charge-related preference on the **m** and **a** surfaces suggests that they are not affected by sector zoning and can thus be regarded as the “neutral” sector. The convergence of the **c**⁺ and **c**⁻ sectors toward this composition appears to confirm such an assignment. As such, this sector can be expected to preserve the “cleanest” record of the changing conditions in the growth environment of the tourmaline without the complicating interactions related to sector-zoning-induced element preference. It further provides a compositional zone that can be compared directly to tourmaline grains that do not display sector zoning.

Although we have not modeled the crystallography of the **o**-face in detail, its non-parallel orientation to the **c**-axis will result in different element preferences on the **c**⁺ and **c**⁻ growing **o**-faces, as it will be affected by the different dipolar surface charge on the Si₆O₁₈-ring. However, the disparity in surface expression of the X-site between **c**⁺ and **c**⁻ growth surfaces is absent for the **o**-face, and no preference is expected on the X-site based on site morphology.

Because of the possibility of asymmetric sector zoning developing on the **o**-faces as well, we believe that the five sectors present in the SY-4 sample (Figs. 4c and 6) result from a combination of **r**- and **o**-face sector zoning. Given that X-site morphology does not appear to play a role for the **o**-face, the compositional differences can be expected to be more pronounced for the **r**-face sectors than for the **o**-face sectors. As no assignment of **r**- and **o**-faces is possible at present, unfortunately this cannot be verified.

CONCLUSIONS AND IMPLICATIONS

The crystallography and compositional sections above show that different tourmaline growth faces have different element preferences, and the decoupling that occurs between chemically similar elements in terms of charge and ionic radius, further indicates that the sectors are not simple mirror images, controlled by the same, but oppositely acting, process. Given the crystallography, we believe sector zoning to be a combined effect of lattice site morphology on the different growth faces and dipolar surface charge related to the systematic orientation of the tetrahedral sites. Preferential incorporation of an element on a growth surface will place constraints on the morphology of

the surrounding crystal sites and thus control the preference of elements on the next growth level. Similarly, charge balance will have to be preserved and can be expected to have a long-range impact on element preference on neighboring sites. This will result in “diffuse” exchange vectors for the different sectors, as has been observed for the tourmalines studied here.

The result of element preference on the various growing faces is the development of three hourglass-shaped sectors, with distinct compositions in terms of major and trace elements. These differences are commonly the same order of magnitude as the variations due to compositional growth zoning. Although we do not imply that all tourmalines will display the features outlined here, the extent of compositional variation does suggest that hourglass sector zoning cannot be ignored, and a proper assessment of tourmaline chemistry should include an assessment of its 3D zoning structure.

ACKNOWLEDGMENTS

We thank Pim van Geffen for his introductory work on the tourmalines of the French Massif Central, which was the incentive for this study. V.vH. acknowledges financial support through a University of Bristol strategic postgraduate scholarship. This work was supported by a NERC small research grant. The Utrecht ICP-MS laboratory receives support from the Netherlands Organisation of Scientific Research (NWO).

REFERENCES CITED

- Barton, R., Jr. (1969) Refinement of the crystal structure of buergerite and the absolute orientation of tourmalines. *Acta Crystallographica B*, 25, 1524–1533.
- Bebout, G.E. and Nakamura, E. (2003) Record in metamorphic tourmalines of subduction-zone devolatilization and boron cycling. *Geology*, 31, 407–410.
- Carlson, W.D. (2002) Presidential Address: Scales of equilibrium and rates of equilibration during metamorphism. *American Mineralogist*, 87, 185–204.
- Deksissa, D.J. and Koeberl, C. (2002) Geochemistry and petrography of gold-quartz-tourmaline veins of the Okote area, southern Ethiopia: implications for gold exploration. *Mineralogy and Petrology*, 75, 101–122.
- Donnay, G. (1977) Structural mechanisms of pyroelectricity in tourmaline. *Acta Crystallographica A*, 33, 927–932.
- Dyar, M.D., Wiedenbeck, M., Robertson, D., Cross, L.R., Delaney, J.S., Ferguson, K., Francis, C.A., Grew, E.S., Guidotti, C.V., Hervig, R.L., Hughes, J.M., Husler, J., Leeman, W., McGuire, A.V., Rhede, D., Rothe, H., Paul, R.L., Richards, I., and Yates, M. (2001) Reference Minerals for Microanalysis of Light Elements. *Geostandards Newsletter*, 25, 441–463.
- Ford, W.E. and Dana, E.S. (1932) A textbook of mineralogy, Fourth Edition, 851 p. John Wiley and Sons, New York.
- Hawthorne, F.C. (2002) Bond-valence constraints on the chemical composition of tourmaline. *Canadian Mineralogist*, 40, 789–797.
- Hawthorne, F.C. and Henry, D.J. (1999) Classification of the minerals of the tourmaline group. *European Journal of Mineralogy*, 11, 201–215.
- Henry, D.J. and Dutrow, B.L. (1992) Tourmaline in a low grade clastic metasedimentary rock: an example of the petrogenetic potential of tourmaline. *Contributions to Mineralogy and Petrology*, 112, 203–218.
- (1996) Metamorphic tourmaline and its petrologic applications. In E.S. Grew and L.M. Anovitz, Eds., *Boron: Mineralogy, Petrology and Geochemistry*, 33, p. 503–557. Reviews in Mineralogy, Mineralogical Society of America, Chantilly, Virginia.
- (2001) Compositional zoning and element partitioning in nickeloan tourmaline from a metamorphosed karstbauxite from Samos, Greece. *American Mineralogist*, 80, 1130–1142.
- Henry, D.J. and Guidotti, C.V. (1985) Tourmaline as a petrogenetic indicator mineral: an example from the staurolite-grade metapelites of NW Maine. *American Mineralogist*, 70, 1–15.
- Henry, D.J., Kirkland, B.L., and Kirkland, D.W. (1999) Sector-zoned tourmaline from the cap rock of a salt dome. *European Journal of Mineralogy*, 11, 263–280.
- Hollister, L.S. (1970) Origin, mechanism, and consequences of compositional sector zoning in staurolite. *American Mineralogist*, 55, 742–766.
- Hollister, L.S. and Gancarz, A. (1971) Compositional sector-zoning in clinopyroxene from the Narce Area, Italy. *American Mineralogist*, 56, 959–979.
- Kawakami, T. (2001) Boron depletion controlled by the breakdown of tourmaline in the migmatite zone of the Aoyama area, Ryoke metamorphic belt, southwestern Japan. *Canadian Mineralogist*, 39, 1529–1546.
- Keller, P., Roda Robles, E., Pesquera Perez, A., and Fontan, F. (1999) Chemistry, paragenesis and significance of tourmaline in pegmatites of the Southern Tin Belt, central Namibia. *Chemical Geology*, 158, 203–225.
- Litvin, M.A., Platonov, A.N., and Khomenko, V.M. (1986) Effect of titanium isomorphic impurity on the colour and pleochroism of hornblende. *Mineralogicheskii Sbornik Lvov*, 40, 30–36.
- Medaris, L.G., Jr., Fournelle, J.H., and Henry, D.J. (2003) Tourmaline-bearing quartz veins in the Baraboo quartzite, Wisconsin: occurrence and significance of foitite and “oxy-foitite”. *Canadian Mineralogist*, 41, 749–758.
- Nakano, T. and Nakamura, E. (2001) Boron isotope geochemistry of metasedimentary rocks and tourmalines in a subduction zone metamorphic suite. *Physics of the Earth and Planetary Interiors*, 127, 233–252.
- Onasch, C.M. and Vennemann, T.W. (1995) Disequilibrium partitioning of oxygen isotopes associated with sector zoning in quartz. *Geology*, 23, 1103–1106.
- Rustemeyer, P. (2003) *Faszination Turmalin*, 309 p. Spektrum Akademischer Verlag, Berlin. ISBN: 3827414245
- Sperlich, R. (1990) Zoning and crystal chemistry of tourmalines in prograde metamorphic sequences of the Central Alps, 51 p. PhD thesis, University of Basel, Switzerland.
- Sperlich, R., Gieré, R., and Frey, M. (1996) Evolution of compositional polarity and zoning in tourmaline during prograde metamorphism of sedimentary rocks in the Swiss Central Alps. *American Mineralogist*, 81, 1222–1236.
- Tindle, A.G., Breaks, F.W., and Selway, J.B. (2002) Tourmaline in petalite-subtype granitic pegmatites: evidence of fractionation and contamination from Pakeagama Lake and Separation Lake areas of northwestern Ontario, Canada. *The Canadian Mineralogist*, 40, 753–788.
- Torres-Ruiz, J., Pesquera, A., Gil-Crespo, P.P., and Velilla, N. (2003) Origin and petrogenetic implications of tourmaline-rich rocks in the Sierra Nevada (Betic Cordillera, southeastern Spain). *Chemical Geology*, 197, 55–86.
- Tracy, R.J. (1982) Compositional zoning and inclusions in metamorphic minerals. In J.M. Ferry, Ed., *Characterization of Metamorphism through Mineral Equilibria*, 10, p. 355–397. Reviews in Mineralogy, Mineralogical Society of America, Chantilly, Virginia.
- Voll, G. (1969) *Klastische Mineralien aus den Sedimentserien der Schottischen Highlands und ihr Schicksal bei aufsteigender Regional- und Kontaktmetamorphose*. Habilitationsthese, Technische Universität Berlin.
- von Goerne, G., Franz, G., and Wirth, R. (1999) Hydrothermal synthesis of large dravite crystals by the chamber method. *European Journal of Mineralogy*, 11, 1061–1078.
- Watson, E.B. (1996) Surface enrichment and trace-element uptake during crystal growth. *Geochimica et Cosmochimica Acta*, 60, 5013–5020.
- Watson, E.B. and Liang, Y. (1995) A simple model for sector zoning in slowly grown crystals: Implications for growth rate and lattice diffusion, with emphasis on accessory minerals in crustal rocks. *American Mineralogist*, 80, 1179–1187.

MANUSCRIPT RECEIVED FEBRUARY 15, 2005

MANUSCRIPT ACCEPTED OCTOBER 19, 2005

MANUSCRIPT HANDLED BY ROBERT DYMEK